

Chapter 11

Probing Microsecond Reactions with Microfluidic Mixers and TCSPC

Sagar V. Kathuria and Osman Bilsel

Abstract Probing the in vitro kinetics and dynamics of macromolecules involved in biological processes is important for discerning their mechanism and function. These dynamics span the sub-microsecond to millisecond and longer timescales. In addition to resolving dynamics and kinetics, structural characterization of non-equilibrium intermediates over these time scales is often desired. In this chapter, we review recent advances in microfluidic mixing methods (both low-Reynolds laminar and chaotic/turbulent mixers) for initiating biochemical reactions and provide an overview of the interfacing of these techniques with time-correlated single photon counting (TCSPC) fluorescent detection methods. We focus on approaches in which both a kinetic reaction time axis and a TCSPC time axis are simultaneously monitored, often referred to as a “double kinetic” experiment. Methods for measurement and analysis of these experiments are presented in which the TCSPC time axis corresponds to fluorescence lifetimes, time-resolved FRET or time-resolved anisotropy. An overview of matrix methods, such as singular value decomposition, and maximum entropy methods for data analysis are also reviewed.

11.1 Introduction and Overview

A wide range of timescales are involved in biological processes, ranging from sub-microseconds for helix formation, to milliseconds for translation of an mRNA to a chain of amino acids and, in some cases, seconds for the folding of the chain to a functional specific three-dimensional structure. An overview is given in Fig. 11.1. A goal of the biophysicist is to understand the thermodynamics and mechanism of how these and related processes occur. A structural probe that a biophysicist can

S.V. Kathuria · O. Bilsel (✉)

Department of Biochemistry and Molecular Pharmacology, University of Massachusetts Medical School, Worcester, MA 01605, USA
e-mail: osman.bilsel@umassmed.edu

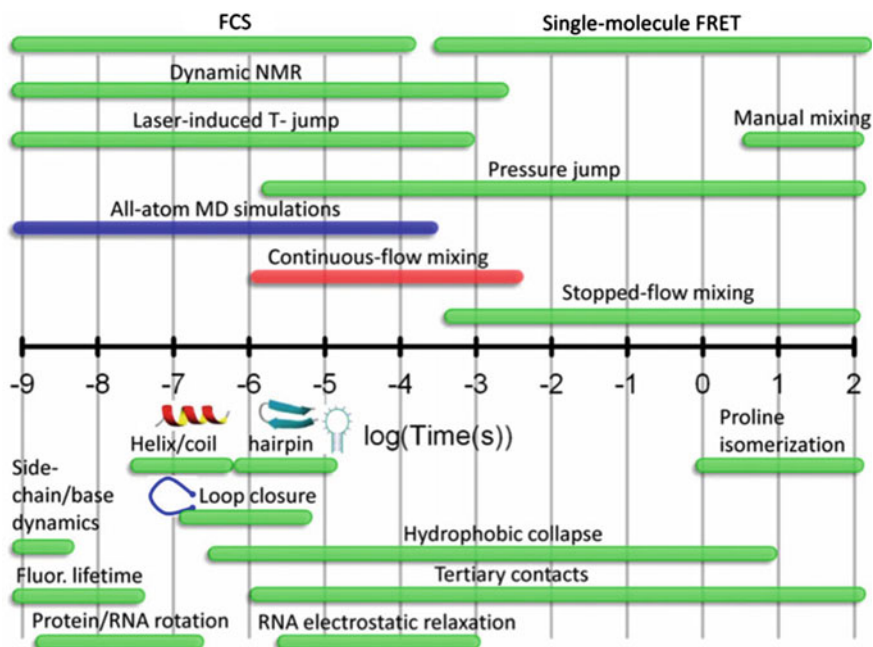


Fig. 11.1 Timescales for macromolecular dynamic processes (*lower half*) and techniques used to probe them (*upper half*). Copyright—2011 Wiley Periodicals, Inc. [31]

use with a time resolution to match the biological/biochemical process is a critical tool for revealing the underlying physics.

An expansive set of tools have been used to achieve a mechanistic and structural understanding of protein-protein, protein-RNA, and protein-DNA interaction, or protein folding and RNA folding. It is important to recognize the complementarity and synergy of many of these techniques. For example, in the case of protein folding, the design of a FRET pair for probing folding dynamics benefits significantly from the availability of a native crystal structure, radius of gyration measurements of the native and denatured state ensembles and residue level hydrogen-deuterium exchange protection information. The present overview of microsecond mixing interfaced with TCSPC is presented with this context in mind, that it can be a valuable tool in the toolkit of the biophysicist. It is also worth noting that numerous other complementary techniques are available with significantly greater time resolution than microfluidic mixing (Fig. 11.1), [31] such as temperature-jump, [14, 20, 24, 30, 44, 53, 67] NMR relaxation methods [28, 51] and FCS, [17, 18] but these have their own limitations with respect to initiation of the reaction and appropriateness for a given protein. The microfluidic methods discussed in this review are ideal for kinetic reactions initiated by a dilution reaction, as in the case of protein folding, [62] RNA folding, [50] or enzymatic reactions [34] in which a

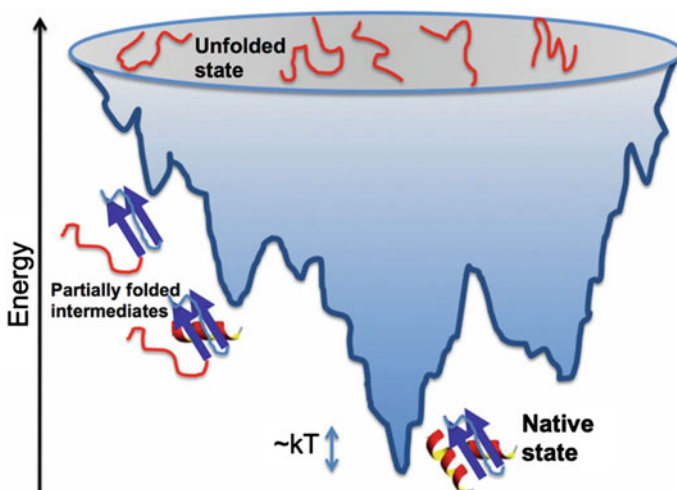


Fig. 11.2 Cartoon representation of the energy landscape for a protein. Some partially folded states are rarely accessed in equilibrium experiments. Non-equilibrium kinetic methods are therefore advantageous in studying them

reagent, such as ATP or an analogue, is added. For protein folding studies, the mixing studies provide a means for studying high-energy partially folded structures that are transiently populated as an approximately random-coil polypeptide folds to its native structure. The mixing approaches are able to achieve relatively high populations of these high-energy states, which may have too low of an equilibrium population for single-molecule studies for proteins with large stability, see Fig. 11.2.

11.1.1 Micromachining Advances Usher in a New Era

Although microsecond mixing devices have appeared in the literature for over three decades (without a dramatic improvement in mixing times) [33], they had not been widely adopted by the biophysics and enzymology researchers, who have favoured the more established stopped-flow method with its millisecond time resolution limitation. Over the past decade and a half, however, advances in micromachining methods (e.g., laser machining, photolithographic methods and DRIE etching) have enabled smaller micron-sized features and more intricate patterns to be machined. The devices have also been increasingly more robust, and ushered in new mixing techniques, such as laminar and chaotic mixing, in addition to the more traditional turbulent mixing methods [41, 54].

11.1.2 Concurrent Advances in TCSPC

Concurrent with developments of microfluidic based mixing devices in the late 1990s and early 2000s came the introduction of compact PCI-based high-speed TCSPC electronics. The higher counting rates possible with these PC-based TCSPC cards, their multi-dimensional recording capabilities [2, 3] (see Chap. 1) and high-repetition rate lasers made kinetic experiments, particularly of the ‘double-kinetic’ variety, [7, 9] (simultaneously performing reaction kinetics and TCSPC based time-resolved fluorescence kinetic) more accessible. These experiments, and their counterparts using camera-based detection [35], allowed researchers to probe millisecond timescale kinetic reactions using lifetime detected FRET. These developments allowed users to obtain not just an average end-to-end intramolecular distance for a given set of donor-acceptor labelled residues of a protein but to also obtain, via Laplace inversion, the time evolution of a distance distribution during a biochemical reaction [35].

11.1.3 Merging Microfluidics and TCSPC

The availability of continuous-flow microfluidic mixers opened the possibility of bringing the time-resolution of the ‘double-kinetic’ experiment into the microsecond time range. The availability of performing TCSPC-based lifetime-resolved FRET and anisotropy studies is significant in that many fundamental events, such as the formation of loops and hairpins of proteins [15, 26, 47, 67], and the folding of some globular proteins [37, 71, 72] occur on this timescale.

11.1.4 Matching Simulation and Experiment

The accessibility of the microsecond time regime in experiments has been paralleled over the past decade with complementary advances in computational molecular dynamics simulations. All-atom simulations can now be performed on proteins greater than 100 amino acids and extend into the millisecond timescale [40, 43]. The overlap between experiment and simulations allows validation of the simulations and provides atomistic insight into the mechanism governing the folding process and dynamics of a globular protein. The availability of distance distributions from lifetime-based FRET data [13] (see Chap. 7) obtained from TCSPC-based measurements in microfluidic devices, as discussed later in this chapter, can be a useful metric for comparing with simulations.

In this review, an overview of microfluidic devices interfaced with TCSPC will be presented, with an emphasis on experimental details and data analysis. This area

is rapidly evolving, and the material presented here will perhaps foster new ideas and approaches for structural measurements of biological complexes in the microsecond time range.

11.2 Microfluidic Mixing Methods

Microfluidic mixers with microsecond time resolution have typically followed two general approaches (Fig. 11.3).

In one case, the mixer operates in the laminar regime and the mixing is accomplished by focusing of a central sheath of flow to a width of approximately $0.1 \mu\text{m}$. Diffusion of the solvent molecules across this narrow sheath can occur on the microsecond timescale. These mixers are very efficient, allowing full experiments to be conducted with femtomoles of samples when used with a confocal microscope. The central $0.1 \mu\text{m}$ (or narrower) wide sheath is narrower than the sample volumes but this is not a serious limitation for fluorescence experiments, especially if a confocal instrument with a high numerical aperture objective is used. For coaxial laminar mixers, the small dimensions of the central sheath are an advantage as there is less out-of-focus light because the central sheath is less than the dimensions of the confocal volume [27]. By appropriate selection of the flow stream, a macroscopic observation volume is attainable for laminar flow mixers [22]. As shown in Fig. 11.4, the central sheath is selected and expanded in an effort to slow the flow rate sufficiently for single-molecule studies. Spectroscopic and kinetic studies have been performed with laminar mixers in the visible [22, 27, 52] and ultraviolet wavelength region [41, 49] (with extrinsic and intrinsic chromophores of proteins, respectively)

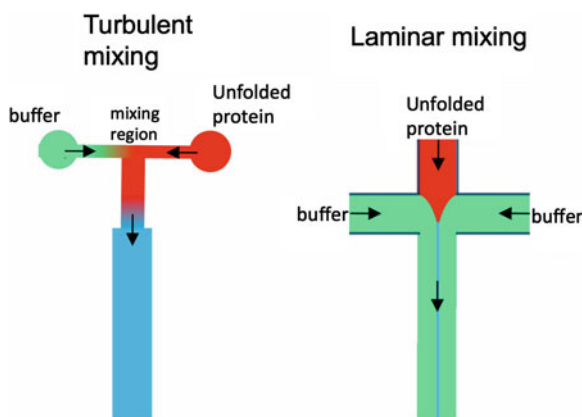


Fig. 11.3 Schematic overview of turbulent/chaotic and laminar mixing approaches to microsecond mixing. Channel widths are $\sim 10 \mu\text{m}$ for laminar mixers and $30\text{--}100 \mu\text{m}$ for turbulent/chaotic mixers. The central sheath in the hydrodynamically focused laminar mixer is $\sim 0.1 \mu\text{m}$. Copyright © 2011 Wiley Periodicals, Inc. [32]

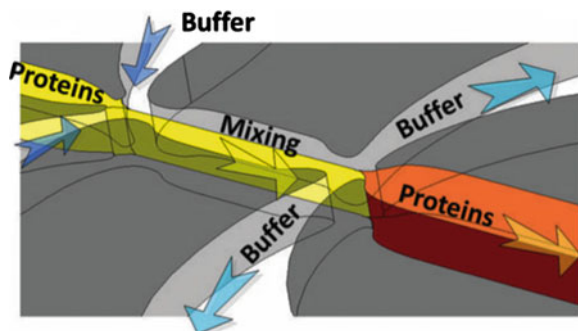


Fig. 11.4 A laminar mixer covering the 200 μ s to seconds time range suitable for TCSPC and single-molecule studies. A 20 nm central sheath (yellow) is picked out of the flow and expanded (orange) to slow the flow rate. Reprinted by permission from [22]. Copyright (2011)

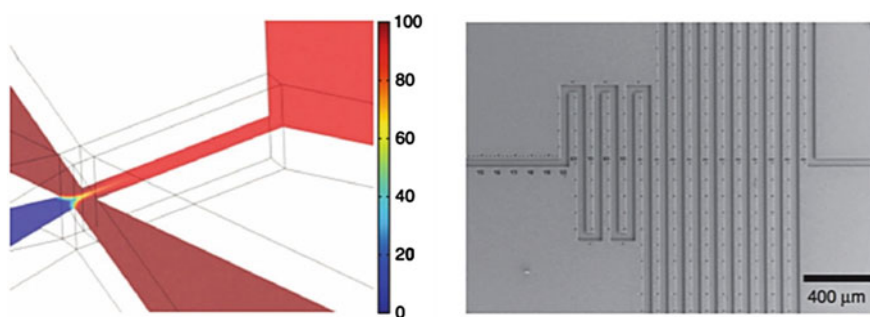


Fig. 11.5 An alternative simpler laminar mixer covering the ms to minutes time range suitable for TCSPC and single-molecule studies. The solutions mix in a 2.5 μ m central channel (yellow to red transition) before expanding to \sim 40 μ m in the observation channel. The flow velocity is \sim 1 μ m/ms. Reprinted by permission from [70]. Copyright (2013)

with both ensemble and single-molecule experiments. However, these experiments have not been used with TCSPC detection.

Another popular approach to microsecond mixers relies on turbulent or chaotic mixing [33, 57]. Two solutions flowing at a fairly high flow rate (10–100 mL/min) in channels of 50–250 μ m width are brought into contact in a way that generates Reynolds numbers on the order of several thousand (Fig. 11.5).

The solution breaks up such that the largest eddies are on the order of 0.1 μ m, allowing diffusion, and mixing, to occur on the tens of microsecond timescale. These mixers tend to consume significantly more material than laminar mixers but allow a larger volume (and thus more signal) to be detected. The larger sample region makes these devices straightforward to interface with ensemble TCSPC setups. However, the high flow rates in these mixers give rise to very low residence times for sample molecules in the focal volume (\sim few microseconds) and make them less than ideal for single-molecule measurements.

The early capillary mixers used steady-state fluorescence detection [56, 60], but an early report by the Rousseau group showed that interfacing of a stainless steel mixer to a TCSPC detection setup could be readily accomplished [64]. An optical quality quartz cuvette mounted on the T-shaped mixer with $250 \times 250 \mu\text{m}^2$ channels achieved a mixing time of $\sim 400 \mu\text{s}$. A subsequent study using laser machined mixers constructed from $127 \mu\text{m}$ thick Kapton (polyimide) or PEEK (poly-ether-ether-ketone) used an epifluorescence detection arrangement with a TCSPC detection setup. Using this setup, approximately 100 TCSPC decay traces of horse heart cytochrome *c* were obtained over a 30–1200 μs range along the time range of the folding reaction [10].

A variety of mixers relying on split-and-recombine and/or flow obstructions that operate at Reynolds numbers in between the laminar and turbulent regimes have been reported [42, 59, 68]. While these “chaotic mixers” generally do not produce mixing on the same timescales as the turbulent mixing or hydrodynamic flow focusing techniques, they operate at relatively lower flow rates than the turbulent mixers and have larger detection volumes than the flow focused laminar mixers. These mixers can be easily interfaced with fluorescence detection using total intensity and TCSPC for both ensemble and single molecule techniques [21, 70]. An illustrative example is shown in Fig. 11.5, where mixing is achieved in a $2.5 \mu\text{m}$ wide channel before widening of the completely mixed solution. This approach slows the flow sufficiently for single-molecule experiments and also enables a large uniform volume to be used for various types of spectroscopy. Lastly, these mixers can achieve longer timescales ranging from a few hundred microseconds to minutes by introduction of a serpentine pattern [70]. While these timescales are easily accessible by most modern stopped-flow devices, the mixing efficiency of chaotic mixers is far superior to that of stopped-flow devices, consuming significantly less material. These devices also operate under lower turbulence and pressure regimes. Further, as the sample is in continuous flow mode, photobleaching is seldom a problem.

11.2.1 Materials

The last few years have seen significant advances in new mixer designs, facilitated in part due to user-friendly off-the-shelf simulation software and the availability of micromachining capabilities. Photolithography followed by etching is widely being used for micromachining of silica wafers [70] that are readily used in hydrodynamic flow focusing laminar mixer devices. A range of materials like quartz cover slips and silicon based polymer materials, PDMS, PMMS, POM, etc. can be used as window material on these chips for spectroscopic applications under low-pressures.

The higher pressures in turbulent flow mixing techniques prevents the use of delicate window materials and is generally circumvented by separating the mixing, which is performed in metal or PEEK mixers, from the observation channels. The optical quality of quartz along with its inert nature makes it ideal for most mixer

types. The use of a femtosecond painting method for micro-etching quartz, developed by Bado and coworkers [8] has enabled the use of fused “single piece” quartz mixers [31, 33] with virtually no design limitations even under high pressures.

11.2.2 Optimization of Mixer Designs by Simulation

Robust commercially available computational fluid dynamics packages, e.g. COMSOL (Fig. 11.6) and ANSYS/Fluent, have led to systematic optimization of various mixer design parameters to achieve the highest mixing efficiencies at the lowest flow rates possible [16, 42, 46, 63]. Of the parameters optimized for various flow geometries, most groups have found that constricting the flow path at the point of mixing of two fluids in conjunction with an obstruction in the form of sharp turns

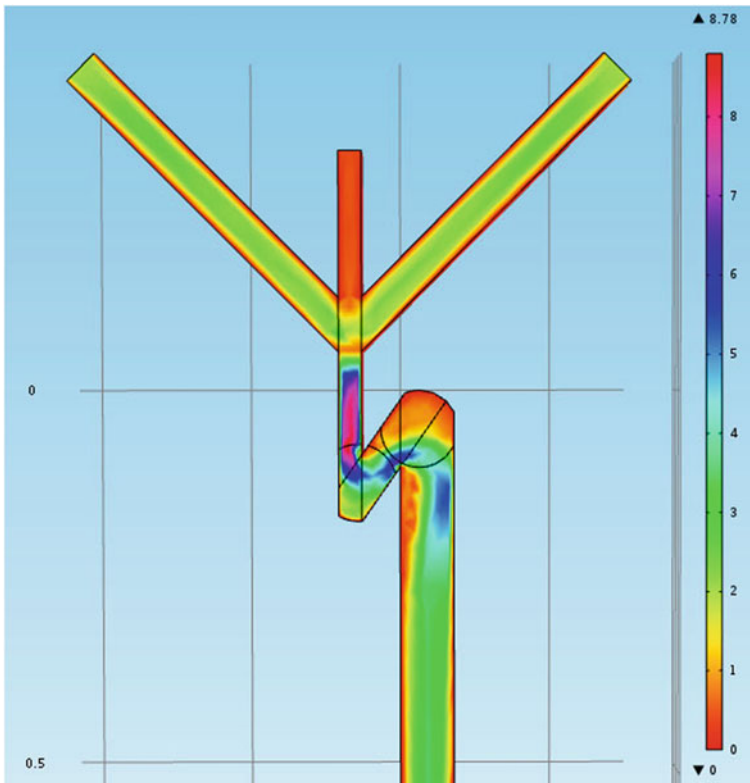


Fig. 11.6 Simulation using COMSOL. Fluid velocities at different positions along the channel are shown. The two side input channels ($50\ \mu\text{m}$) are flowing at $2\ \text{m/s}$ and the central channel ($30\ \mu\text{m}$) flowing at $0.4\ \text{m/s}$. The flow velocity is uniform within $0.5\ \text{mm}$ from the point of mixing

is the most efficient under non-laminar flow conditions. Under laminar conditions, the SAR, serpentine and herringbone patterned mixers appear to be more effective as they provide greater opportunity to increase the contact surface area between the two fluids and enhance passive diffusion.

One of the major limitations of continuous-flow mixers is that they have historically required either higher concentrations (laminar mixers) or amounts (turbulent mixers) of sample relative to stopped-flow experiments. Chaotic mixers can potentially overcome both of these limitations. Simulations play a significant role in developing geometries to optimize flow paths to achieve faster and more efficient mixing and to minimize dead spaces to reduce the priming sample volume required for uniform flow.

11.3 Interfacing Microfluidic Chips with TCSPC

11.3.1 Advantages of TCSPC

The motivation for interfacing microsecond mixing devices with TCSPC instrumentation [2, 3] stems from several factors. For FRET studies, the advantages offered by TCSPC can be substantial, see Chaps. 7 and 8 of this book. By collecting the time-resolved decay of the donor (and, where available, the acceptor), the user is able to record the average distance as well as the distribution of distances between a donor and acceptor fluorescent label on the molecule of interest. Therefore, by having the TCSPC axis, the user can distinguish whether the average FRET efficiency arises from a single population or multiple sub-populations. Additionally, the average FRET efficiency calculated from the donor lifetime is more accurate than that obtained through steady-state methods [13], see Chaps. 7 and 8. In steady-state methods, matching the concentrations of donor-only and donor-acceptor controls is a source of error in the average FRET efficiency determination. The fluorescence lifetime, however, is independent of concentration unless the concentration is sufficiently high that higher order oligomers, exciplexes or other quenching reactions are introduced. Furthermore, the theoretical standard deviation of a lifetime measurement is \sqrt{N}/N for N photons [36], where N is on the order of 10^6 . TCSPC comes very close to this ideal value. This latter point is helpful for the continuous-flow TCSPC experiment as the first moment of the lifetime decay can be used as a cross-check to confirm the intensity normalization, as will be discussed further below. Advantages of TCSPC detection also extend to anisotropy measurements, where the measurement of rotational correlation times can be very useful for assessing local structure and hydrodynamic size, see Chap. 12 of this book.

With the availability of compact high-repetition rate lasers over a broad spectral range and PC-based TCSPC cards, the adoption of TCSPC detection for microfluidic mixing devices is likely to increase. Below we present some of the instrumentation and design considerations in the practical application of continuous-flow microfluidic mixers with TCSPC detection.

11.3.2 Instrumentation

The basic setup for continuous-flow TCSPC experiments is shown in Fig. 11.7.

The setup is essentially that of an epi-fluorescence microscope equipped with an xy-scanning stage. The implementation currently in use at the University of Massachusetts Medical School utilizes the doubled or tripled output of a Ti:sapphire laser operating at 76 MHz repetition rate as the excitation source. The repetition rate is dropped to 3.8 MHz using an acousto-optical pulse picker for most experiments to allow more accurate determination of longer lifetimes (e.g., >4 ns), such as, experiments using Trp and cyano-Phe [1, 58, 65] fluorescence. The 3.8 MHz is due to the limitation of our pulse picker, in fact a repetition rate on the order of 20 MHz would be more appropriate. A laser power of several hundred μW is available but only a power of ~ 100 μW is needed for excitation.

For experiments at 290–295 nm, a dichroic filter (FF310, Semrock Inc., Rochester, NY) is used to reflect the excitation to the sample. A single element plano-convex lens (35 mm focal length) is used to focus the excitation to an approximately 20 μm spot. Although a higher numerical aperture objective can be used, maintaining a constant intensity along the length of the 30 mm flow channel

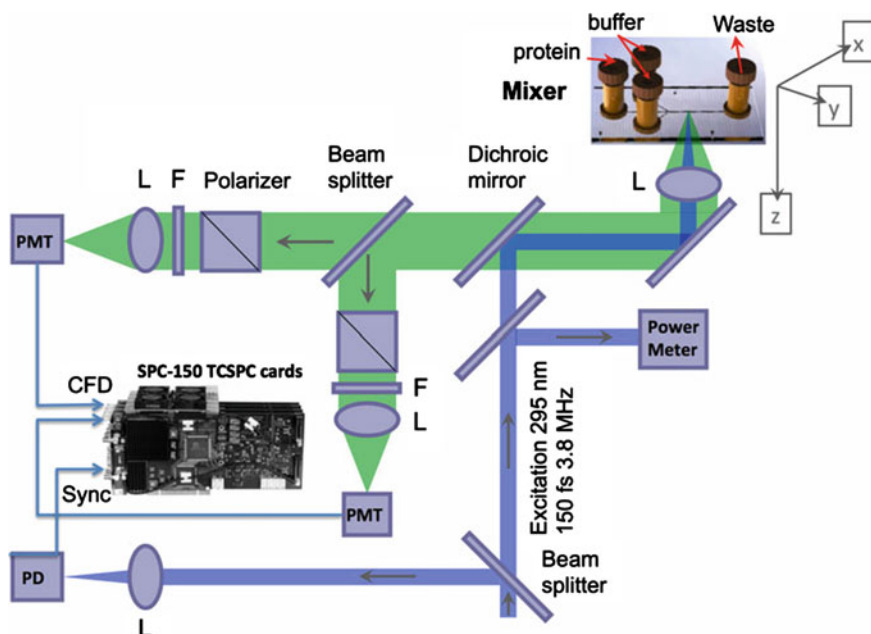


Fig. 11.7 Schematic of epifluorescence setup for continuous-flow TCSPC measurements. Abbreviations: *L* lens, *F* bandpass filter, *PMT* photomultiplier tube, *PD* fast photodiode. The flow channel is ~ 50 – 70 μm wide, ~ 50 – 100 μm deep and 30 mm long. The flow velocity is $\sim (30 \mu\text{s}/\text{mm})^{-1}$

becomes more challenging. A thin quartz plate is used to pick off a fraction of the excitation beam and directed into a power meter.

The microfluidic mixer is mounted horizontally onto a xy-stage (Ludl Biopoint 2). A positioning accuracy of a few microns is sufficient for channels that are $>30\ \mu\text{m}$ in width.

The fluorescence from the sample solution inside the channel is collimated, and transmitted by the dichroic mirror. The fluorescence light is further split in two components, which are projected onto UV sensitive PMT modules (PMH100-6) or microchannel plate (MCP) PMTs. The outputs of the PMTs are fed into two separate SPC150 TCSPC cards [3].

Wavelength selection is accomplished via bandpass filters (e.g., FF357/44 for tryptophan experiments), although the option of using a monochromator is available. The greater spectral width and excellent out-of-band rejection available with bandpass filters renders them very practical. A motorized Glan-Taylor polarizer at magic-angle is present in each detection path. The polarisers can be set to detect parallel and perpendicular polarisation components or for magic-angle detection. Magic-angle detection rejects contributions from chromophore reorientational dynamics from the decay data. Please note that the commonly used magic-angle of 54.7° strictly applies only for excitation and detection in parallel beams of light. The NA of our detection optics is 0.25, where the magic angle is still very close to the value for parallel beams. For excitation and detection at higher NA the magic angle decreases and approaches 45° for $\text{NA} = 1$ [19].

11.3.3 Alignment

The initial setup for the experiment consists of aligning the excitation beam, the detection path and in locating the start, stop and centre of the channel. Alignment of the excitation and detection paths is analogous to that of a confocal microscope without the pinhole. A concentrated dye solution is placed on the xy-stage instead of the mixer to view the fluorescent light path. The dichroic also transmits a small amount of the excitation light, which is useful for alignment purposes.

The precise location of the mixer flow channel is accomplished by placing an approximately 10-fold higher concentration of a fluorescent small molecule, appropriate for the experiment excitation and emission wavelengths, in the mixer channel (e.g., N-acetyl-tryptophanamide for tryptophan based experiments). The channel is point-scanned (at $\sim 5\ \mu\text{m}$ resolution) perpendicular to the flow direction at approximately 1 mm intervals along the flow direction to locate the centre of the channel along the 30 mm flow path. A linear least squares fit to the measured centre positions yields the slope and intercept that allows calculation of a lookup table. With a lookup table in hand, an additional point-scan is recorded parallel to the flow channel along the centre. The mid-point of the rise of the signal provides the location of the start of the channel and provides an estimate of the zero-time of the experiment. Because the beam focus diameter is smaller than the channel width, the intensity variation along

the flow channel is small, approximately 5 %, usually caused by the tolerance in thickness of the quartz plates used to construct the mixer. This intensity profile is recorded with each experiment and used to normalize the TCSPC traces at each point along the channel. The mixer is brought into focus in the z-direction by repeated scans perpendicular to the direction of flow while optimizing the signal intensity.

11.3.4 Data Acquisition Protocol

In a typical experiment the sample and control will be placed in separate sample loops. The blank solution (e.g., matching the sample in every respect except without protein) is placed in the pump pushing out the contents of the sample loop. The other pump contains the dilution buffer. The flow rate is on the order of 2–6 mL/min total, although efforts are underway to reduce this volume to below 1 mL/min. Control of the pumps and valves is under computer control.

A typical experiment uses 10 mL sample loops giving a data collection time of approximately 15–20 min for the sample. As the sample flows, a scan is made along the flow direction every minute, consisting of 60–100 points. Although the TCSPC cards can be operated in “continuous-flow” mode, recording photons without any gap, the double time mode tends to be more commonly employed. In the latter mode, at each step along the channel the xy-stage is positioned and TCSPC acquisition for approximately 0.5 or 1 s is individually triggered, keeping the stage stationary during acquisition. The duty cycle is therefore ~50–75 %.

Count rates for these experiments tend to be in the 5×10^4 to $<1 \times 10^5$ cps per detection channel. For an excitation pulse frequency of 3.8 MHz used in our experiments this is well within the range where pile-up is not an issue [2, 3]. Higher count rates may be available with more efficient detectors [4]. Even then, adverse pulse pile-up effects [11] can be avoided by using higher excitation pulse frequency, and by using multiple detectors and parallel TCSPC channels [2, 3].

Data acquisition consists of recording three separate measurements: a blank, sample and control. Each data set consists of approximately 15–20 scans with each scan comprising ~60–100 TCSPC traces with 4096 points in the excited state decay. The experiment is visualized by examining the integrals of the decays (Fig. 11.8).

Traces which overlay are summed. The control scans (e.g., NATA) are summed along the TCSPC axis since only the integrated intensity is used in the normalization. A corrected data set for the sample is therefore obtained according to the following relationship:

$$I_{corr}(t_{kin}, t_{TCSPC}) = \frac{I(t_{kin}, t_{TCSPC}) - Blank(t_{kin}, t_{TCSPC})}{\sum_{t_{TCSPC}} (NATA(t_{kin}, t_{TCSPC}) - Blank(t_{kin}, t_{TCSPC}))}. \quad (11.1)$$

In the above expression the kinetic time axis (corresponding to distance along the flow direction in the channel) is denoted by t_{kin} and the TCSPC time axis is

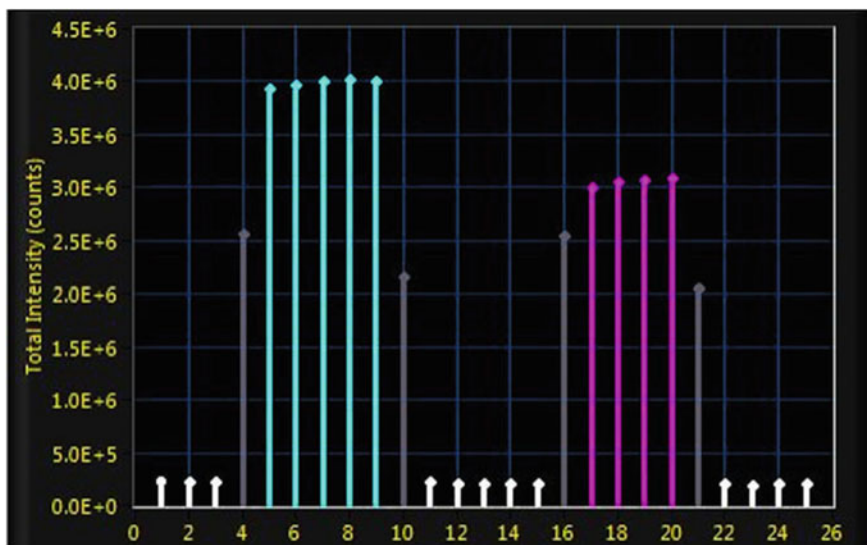
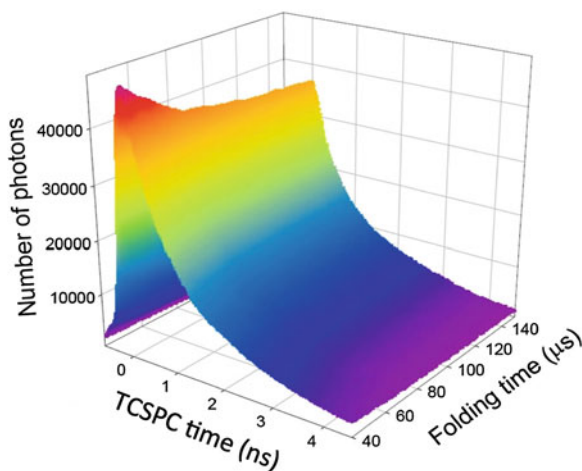


Fig. 11.8 Visualization of the experiment via the total intensity of each scan. The *blue* bars correspond to scans where the control is flowing through the mixer. The *magenta* bars correspond to the protein sample, the *white* bars are the blanks and the *grey* bars correspond to the traces where the sample flow was started or stopped and the entire channel has not reached flow-equilibrium

Fig. 11.9 Representative continuous-flow TCSPC data. Continuous-flow refolding of horse heart cytochrome *c* is shown over the 30–140 μs time range, where the collapse transition takes place. Reprinted from [32], Copyright (2014), with permission from Elsevier



denoted by t_{TCSPC} . The former is in microseconds and the latter in ns. An analysis program with a graphical interface allows the user to analyze a data set in a few minutes, providing rapid feedback on the experiment. A representative data set, collected for horse heart cytochrome *c* is shown in Fig. 11.9.

With binning of several frames, the counts can be on par with what is necessary for distance distribution modelling and maximum entropy analysis, as is discussed further in this chapter.

11.3.5 Point Scanning TCSPC Versus CCD Based Steady-State Acquisition

The point scanning protocol used in these experiments has several pros and cons relative to the CCD based detection that is used by some groups [60]. Other than the advantage of TCSPC based acquisition, the point scanning allows full use of the incident beam intensity, which is very helpful in cases where the experiment is not limited by counting rate and is excitation flux limited. The CCD approach can be advantageous when excitation flux is not limiting. The CCD based approach provides the full kinetics simultaneously for all positions along the channel. The intensity variation along the channel tends to be larger for the CCD based approach but appears to not limit the data quality. The choice of using a CCD based approach or point scanning TCSPC depends on whether the fluorescence decay parameters are desired and the excitation flux available.

11.3.6 Alternative Approaches

Scanning along the flow channel can be avoided by using the multi-channel TCSPC architecture described in Chap. 1, Sect. 1.4.1. The entire flow channel would be illuminated simultaneously, an image of it projected on a multi-anode PMT, and the signals detected by the individual channels of the multi-anode PMT recorded simultaneously. The approach would increase the efficiency of the measurement enormously, and thus decrease the acquisition time and the amount of sample fluid needed for the experiment. A possible problem is that the number of data points along the channel would be limited by the number of PMT channels, typically 16. To spread the 16 data points reasonably over the protein folding time axis the flow speed must be adjusted to the expected folding time. An instrument using the multi-channel PMT technique has not been described yet.

Although the scope of this chapter is on the application of TCSPC, it is worth noting that other recording techniques can also be used for obtaining time-resolved fluorescence decays along a microfluidic microsecond mixer. One option is to use a fast digital oscilloscope (13 GHz bandwidth) in combination with an MCP-PMT, as implemented by Haas and coworkers [29]. An advantage of this approach is that multiple photons can be collected in a single detection channel per laser pulse. This is useful for experiments utilizing low-repetition rate lasers [55]. However, there is no need to use an extremely low repetition rate. For high repetition-rate lasers the

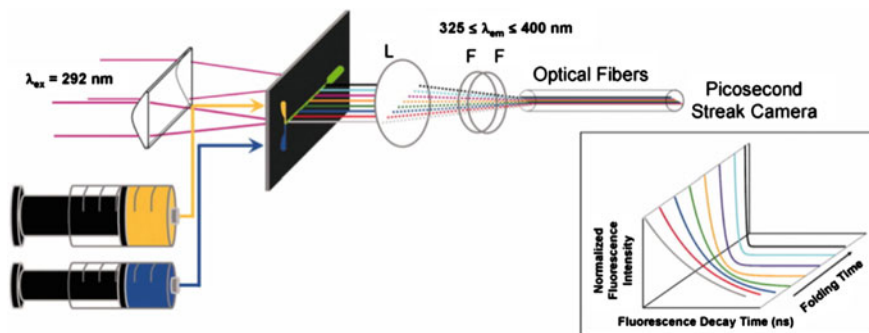


Fig. 11.10 Schematic of streak camera based fluorescence lifetime measurements. Copyright—2006 by The National Academy of Sciences of the USA [35]

problem of detecting multiple photons per laser pulse does not exist. The efficiency of analog recording is lower than for TCSPC, especially if the system is operated at low photon rates. The time resolution is limited by the single-electron response of the detector, not by the transit-time-spread as in the case of TCSPC, see Chap. 1, Fig. 1.4. It is about 300 ps for an MCP PMT, and 1–2 ns for a conventional PMT, compared to 30 and 200–300 ps in the case of TCSPC. Moreover, the current output of an MCP PMT tends to become a limiting factor: If several photons per excitation pulse are detected channel saturation almost certainly causes nonlinearity in the detected decay curves.

Lifetime-based FRET studies using a microsecond mixer were also performed using a streak camera by the Winkler group [35]. The picosecond streak camera allows the entire mixer to be imaged while providing excellent resolution along the excited state fluorescence decay (Fig. 11.10).

Their study provided high signal-to-noise picosecond resolved excited state decays at 25 points in the folding of a cytochrome *c*' four-helix bundle. The dynamic range of the camera allows the full excitation pulse (from an amplified laser) to be used. Other than the cost of the camera, the only limitation for this approach appears to be the coupling of the light into a fibre optic array bundle, which appears to have limited the earliest observation point. It seems likely that these limitations may be readily overcome with more recent microfluidic mixer designs.

11.4 Data Analysis

The continuous-flow TCSPC experiment presents the user with a rich data set, consisting of ~ 40 scans with ~ 100 kinetic time points and 4096 TCSPC time channels in each of the detection channels. One of the challenges is to rapidly evaluate the data set to gauge whether the experimental time window and signal-to-

noise are sufficient and determine if a kinetic process is being observed. For time-resolved FRET and anisotropy experiments, this is done in several stages of analysis with each stage increasing in complexity and rigor. A brief overview of some of the analysis approaches is presented, with an emphasis on FRET and anisotropy data sets.

11.4.1 First Moment

The first moment of the histogram of the photon arrival times (often referred to as the “centre of mass”) provides a quick overview of a data set. The first moment is known to a relative precision of \sqrt{N}/N and is an easy to calculate metric that is also model independent and relatively insensitive to the number of photons. The first moment is calculated according to:

$$\langle \tau \rangle = \frac{\sum_i I_i(t_i - t_o)}{\sum_i I_i} \quad (11.2)$$

where I_i is the photon counts in the i th TCSPC channel, t_i is the TAC time of the i th channel and t_o is the excitation pulse arrival TAC time. This is mathematically equivalent to a quantum yield weighted average lifetime:

$$\langle \tau \rangle = \frac{\sum_i \alpha_i \tau_i^2}{\sum_i \alpha_i \tau_i} \quad (11.3)$$

where α_i is the amplitude of the i th exponential phase with relaxation time constant τ_i .

One potential drawback to the use of the first moment as a metric for kinetic analysis is that it is not rigorously proportional to mole fraction (concentration). Therefore, the time constant(s) of the kinetics can be biased to a lower or higher value depending on the relative quantum yields of the reactants. A workaround is to include the total intensity data $I(t_{kin})$, which has the quantum yield information, and fit it globally with the first moment. Assuming that the amplitudes in (11.3) are linearly proportional to concentration, $\alpha_i = q_i c_i$, for specie, i , the first moment at the reaction time, t_{kin} , can be written as:

$$\langle \tau \rangle(t_{kin}) = \frac{\sum_i q_i c_i(t_{kin}) \tau_i^2}{\sum_i q_i c_i(t_{kin}) \tau_i} \quad (11.4)$$

and the total intensity as:

$$I(t_{kin}) = \sum_i q_i c_i(t_{kin}) \tau_i. \quad (11.5)$$

For a two-state kinetic reaction ($i = 1, 2$),

$$\begin{aligned} c_1(t_{kin}) &= c_1(0)e^{-k \cdot t} \\ c_2(t_{kin}) &= c_2(0)(1 - e^{-k \cdot t}) \end{aligned} \quad (11.6)$$

where k is the rate constant of the reaction, q_i are the relative quantum yields, and c_i , are the concentrations. The parameters q_i and τ_i are globally optimized simultaneously for the two kinetic traces. The approach can be generalized to an arbitrary kinetic mechanism.

This analysis of the first moment is analogous to that proposed previously for the analysis of anisotropy kinetic data [48]. It is worth noting that if the quantum yields are different for the two states the first moment and total intensity will not track each other. For the case where anisotropy and lifetime are collected, the global analysis would also include the steady-state anisotropy data:

$$r(t_{kin}) = \frac{\sum_i q_i c_i(t_{kin}) r_i}{\sum_i q_i c_i(t_{kin})} \quad (11.7)$$

where r_i are the steady state anisotropy values of the states in the kinetic mechanism obtained from the vertical and horizontally polarized data in the customary manner [48]. Similar, to the first moment, the parameters q_i and r_i are globally optimized. The first moment data calculated from the total intensity ($I = V + 2GH$) can also be included in the fitting to improve parameter estimation and kinetic model discrimination.

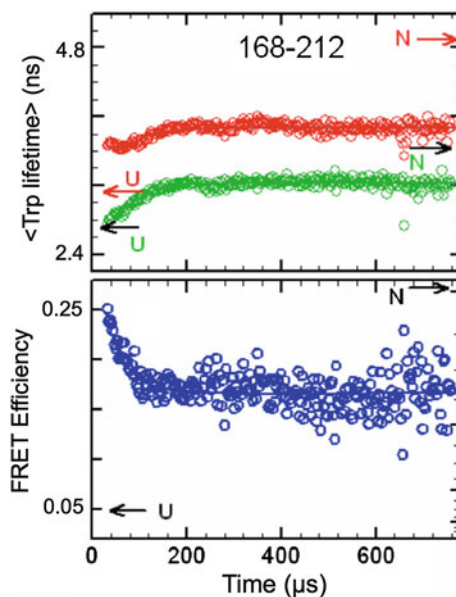
For the case where a FRET efficiency is sought, the average FRET efficiency, E , can be approximated (with the above caveats) from the average lifetimes of the donor-only, $\langle \tau_D \rangle$, donor-acceptor, $\langle \tau_{DA} \rangle$, and $\langle \tau_{DA} \rangle_{App}$, lifetimes:

$$\begin{aligned} \langle \tau_{DA} \rangle_{App} &= x \cdot \langle \tau_{DA} \rangle + (1 - x) \cdot \langle \tau_D \rangle \\ E &= 1 - \frac{\langle \tau_{DA} \rangle}{\langle \tau_D \rangle} = 1 - \frac{\langle \tau_{DA} \rangle_{App}}{x \cdot \langle \tau_D \rangle} + \frac{1 - x}{x} \end{aligned} \quad (11.8)$$

where x represents the acceptor labelling efficiency. If x is less than unity, the measured lifetime of the donor in the presence of the acceptor, $\langle \tau_{DA} \rangle_{App}$, may be related to the true value, $\langle \tau_{DA} \rangle$, via the fractional labelling efficiency, x . An example of a first moment analysis for FRET data on a TIM barrel protein is shown in Fig. 11.11.

Use of the first moment data in practice requires subtraction of the pulse arrival time and consistency in the relative time range (relative the pulse arrival time) used for the calculation. It should also be kept in mind that using the steady-state anisotropy and first moments provides an efficient method of determining the number of kinetic steps but comes at the expense of not fully utilizing the

Fig. 11.11 First moment analysis of FRET data from a TIM barrel protein. The first moment of the donor-only (red) and donor-acceptor (green) labelled protein is shown in the *top panel*. The labelling efficiency corrected FRET efficiency (blue) is shown in the *bottom panel*. Copyright—2008 by The National Academy of Sciences of the USA [69]



information available in the time-resolved FRET and anisotropy data. This information can be obtained alongside the kinetic analysis via a full global analysis, as discussed below.

11.4.2 Global Analysis

Global analysis [6, 7, 9] is a more rigorous approach that involves direct fitting of the raw data. A global analysis allows more stringent testing of a model (e.g., kinetic model and/or distance distribution model) because the linkage of parameters over data sets reduces the number of parameters. The continuous-flow TCSPC data obtained with microfluidic mixers is ideal for this type of analysis although, depending on the extent of the global analysis, can be complicated to set up. In practice, the most robust parameter estimates are obtained if the full raw data set can be parameterized using a kinetic model for the continuous-flow time axis and using a distance distribution or anisotropy decay model for the TCSPC time axis. Below, an overview of a global analysis strategy of time-resolved FRET data is presented.

In one type of global analysis of tr-FRET data, decays from each kinetic time point (e.g., decays corresponding to donor-only and donor-acceptor samples) are globally analyzed using a distance distribution function. In practice, the global analysis is often performed stepwise: the donor-only decay is fit to a sum of exponentials, yielding the fractional amplitudes (α_i), total amplitude ($I_d(0)$) and decay constants (k_{d_i}).

$$I_d(t_{TCSPC}) = I_d(0) \cdot \sum_i^N \alpha_i e^{-k_{di} \cdot t_{TCSPC}} + const \quad (11.9)$$

These parameters are then held fixed in the next step of the analysis, performed on the donor-acceptor decay, in which only the normalized distribution function parameters, $p(k_{ET})$, are allowed to vary:

$$I_{da}(t_{TCSPC}) = \int_0^{\infty} \sum_i^N \alpha_i e^{-k_{di} \cdot t_{TCSPC}} \cdot p(k_{ET}) \cdot e^{-k_{ET} \cdot t_{TCSPC}} + const. \quad (11.10)$$

In the above expressions, α_i is the fractional amplitude of the i th decay component with rate k_{di} , k_{ET} is the energy transfer rate and $p(k_{ET})$ is the energy transfer rate distribution. An assumption in this analysis is that, if the donor has multiple sub-populations with different donor decay rates (e.g. tryptophan), they are assumed to have the same energy-transfer rate distribution. (This assumption is not made in the 2D maximum entropy analysis discussed further below). The energy transfer rate distribution, $p(k_{ET})$, is related to the pair-distance distribution, $p(r)$, according to the Förster equation:

$$r^6 = R_0^6 \cdot \left(\frac{k_{Dave}}{k_{ET}} \right) \quad (11.11)$$

where k_{Dave} is the inverse of the average lifetime of the donor in the absence of the acceptor. The distribution $p(k_{ET})$ is often described by a sum of Gaussian distribution functions:

$$p(r) = \sum_i \frac{a_i}{\sigma \sqrt{2\pi}} e^{-(r-\omega_i)^2/2\sigma_i^2} \quad (11.12)$$

where a_i is the amplitude, ω_i the centre and σ_i the width of the i th Gaussian. The width of the Gaussian can be converted to the full-width at half-maximum by $FWHM = \sigma/2.354$. The adjustable parameters in the non-linear least squares optimization are the amplitude(s), α_i , width, σ_i , and centre, ω_i of the Gaussians and the offset (*const.*) [69]. Distribution functions other than Gaussians may be used. For example, if the distance distribution function of one of the components is expected to correspond to a random-coil, one of the Gaussian functions may be replaced by a worm-like chain model [66]:

$$p(r) = \frac{4\pi a N r^2}{l_c^2 \left(1 - \left(\frac{r}{l_c}\right)^2\right)^{9/2}} \exp\left(\frac{-3l_c}{4l_p \left(1 - \left(\frac{r}{l_c}\right)^2\right)}\right) \quad (11.13)$$

where one fewer parameter is required (the amplitude, a , and the persistence length, l_p) to describe the functional form. The contour length, l_c , is obtained from the number of amino acids, N_{res} ($3.4 \cdot N_{\text{res}}$) and is held fixed.

An extension of this analysis parameterizes both the time axis of the reaction kinetics and the TCSPC time axis in a combined analysis. This was performed, for example, for an associative anisotropy model analysis of the TCSPC axis together with a kinetic folding mechanism [9]. The analysis allows deconvolution of physical parameters (e.g., rotational correlation times, lifetimes, fundamental anisotropy etc.) for individual species in the reaction even if the species is not fully populated at 100 %. A similar approach can be applied to tr-FRET data as well. For example, for a kinetic reaction, where $A_1 \rightleftharpoons A_2 \rightleftharpoons \dots A_n$, the distribution function at any given time is the population weighted linear combination of the distribution functions, $p_i(r)$, of the contributing species, A_i , $i = 1, n$:

$$p(r, t_{\text{kin}}) = \sum_i c_i(t_{\text{kin}}) \cdot p_i(r) \quad (11.14)$$

The populations (concentrations) can be obtained from the solution to the general rate equation:

$$\frac{d\vec{C}(t_{\text{kin}})}{dt} = \hat{S} \cdot \vec{C}(t_{\text{kin}}) = - \sum_{j=1, n; j \neq i} k_{ij} \cdot c_i(t_{\text{kin}}) + \sum_{j=1, n; j \neq i} k_{ji} \cdot c_j(t_{\text{kin}}) \quad (11.15)$$

where C is a vector of concentrations, S is the system matrix and t_{kin} denotes the time along the microsecond reaction kinetics axis (to distinguish from the TCSPC axis). The rate k_{ij} denotes the microscopic rate from species i to species j . In practice, signal-to-noise limits the number of distributions that can be reliably delineated.

11.4.3 Global Analysis with Diffusion of Donor and Acceptor

A further refinement of the global analysis described above takes into account the relative intramolecular diffusion of the donor and acceptor chromophores during the lifetime of the donor excited state [5]. For unfolded proteins and peptides, values of the diffusion constant have ranged from 5 to 15 $\text{\AA}^2/\text{ns}$ [25, 39]. Consideration of diffusion, therefore, becomes significant for highly flexible macromolecules probed with a donor having a long lifetime (>4 ns) and a short Förster distance. A straightforward implementation of diffusion begins with the distance distribution function, $p(r, t_{\text{kin}}, 0)$, and requires solving the diffusion equation for each of the times along the TCSPC time axis to obtain $p(r, t_{\text{kin}}, t_{\text{TCSPC}})$. If the diffusion coefficient is a constant, then, the distribution function at TCSPC time, t_{TCSPC} , is obtained according to a one-dimensional diffusion equation in the absence of a potential,

$$\frac{\partial p(r, t_{kin}, t_{TCSPC})}{\partial t} = D \cdot \frac{\partial^2}{\partial r^2} p(r, t_{kin}, t_{TCSPC}) \quad (11.16)$$

that can be readily solved using finite difference numerical methods.

11.4.4 SVD: Singular Value Decomposition

SVD is a valuable data reduction strategy that provides a quick model-independent assessment of the number of distinguishable lifetime decays or “spectra” in the data. The SVD algorithm reduces the data into the minimum number of orthonormal basis vectors along both, the kinetic time axis, t_{kin} , and the TCSPC time axis, t_{TCSPC} . This is expressed as:

$$A = UWV^T \quad (11.17)$$

where the columns of U represent the kinetic basis vectors, the columns of V are the TCSPC axis basis vectors and W is diagonal matrix containing the singular values. In practice, only the first few basis vectors of U and V are significant, with the remaining vectors being essentially random noise. SVD can, therefore, be used to filter data while knowing exactly what is being thrown out. The sum of the outer product of the first few significant vectors represents a least-squares approximation to the full data. The number of significant basis vectors also gives the user an indication of the minimum number of distinct species contributing to the data. In the example shown in Fig. 11.12, the SVD analysis suggested that only two dominant intermediates were present during the course of the collapse of cytochrome c , arguing for a concerted process [32].

SVD can also be used as an efficient route to a full global analysis. The parameters obtained from a global analysis of the SVD vectors (either the U or the V vectors) can be propagated using the coefficients of the other matrices to reconstruct a full parameter set. Application of SVD to trFRET and time-resolved anisotropy data sets is complicated by the requirements that two data sets need to be analyzed globally and examples of this have not appeared in the literature.

11.4.5 Maximum Entropy

Another model independent analysis approach suitable for fluorescence lifetime, anisotropy and FRET is the maximum entropy method (MEM). The MEM describes a data set (e.g., fluorescence excited state decay) with a distribution of rates, choosing the widest and smoothest distribution that is consistent with the data. MEM starts out with a flat a priori distribution and the amplitude of a given rate deviates from this a priori distribution only as warranted by the data.

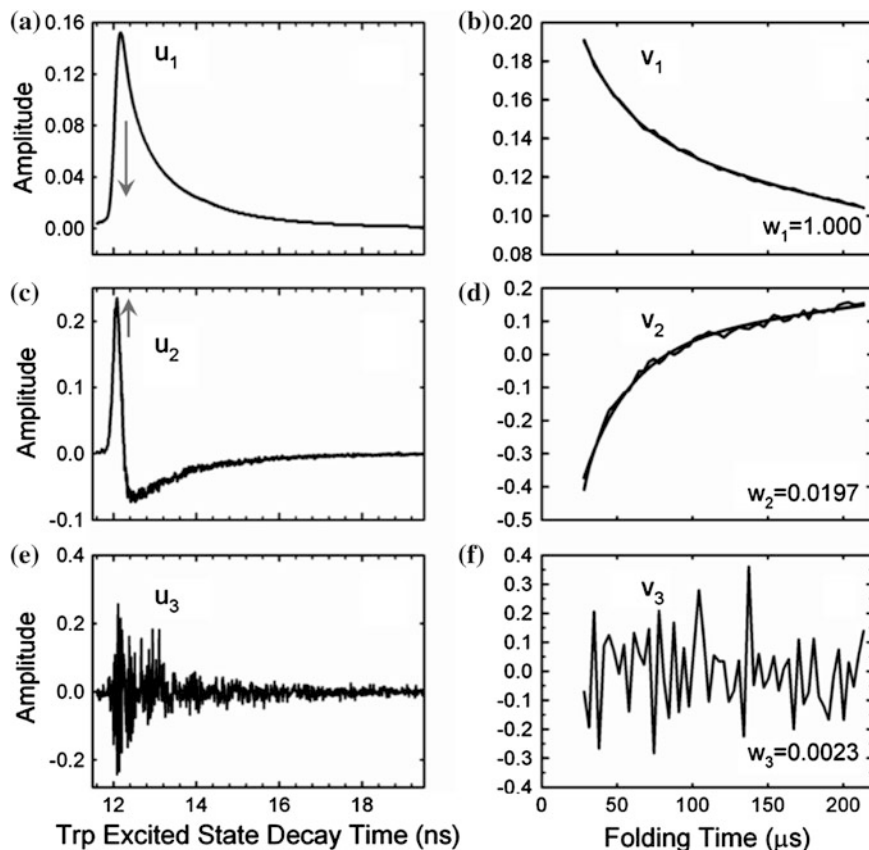


Fig. 11.12 SVD analysis of continuous-flow TCSPC data. The first few columns of the U and V matrices are shown. The remaining columns are essentially noise, similar to the third column. Data correspond to refolding of horse heart cytochrome c shown in Fig. 11.9. Reprinted from [32], Copyright (2014), with permission from Elsevier

The algorithm simultaneously minimizes χ^2 and maximizes the entropy of the distribution, the balance between the two determined by the Lagrange multiplier. An attractive feature of MEM is that it provides the most objective assessment of the true information content of the data [12, 45, 61]. MEM has been widely used in the TCSPC literature for both static and kinetic data [12, 35, 45]. For trFRET data one of the potential applications of MEM is to provide a model independent recovery of the donor-acceptor distance distribution function. Additionally, MEM offers the possibility of avoiding the assumption of the same distance distribution function for each sub-population of the donor excited state.

The ability of MEM to accurately recover the distribution of decay rates has been well established [38]. Extending MEM to time-resolved FRET involves analysis of both the donor and the donor-acceptor excited state decays. This approach parallels

the MEM analysis of time-resolved anisotropy [23]. A concern about degeneracy in the 2D MEM distribution was raised; however, the MEM algorithm proposed by Kumar et al. [38] appears to not be susceptible to this, rendering the approach promising. The donor excited state decay is described according to (11.18):

$$I_d(t_{TCSPC}) = \int_0^{\infty} P(K_d) \cdot e^{-(k_d) \cdot t_{TCSPC}} dk_d \quad (11.18)$$

$$k_d \equiv 1/\tau_d$$

where k_d is defined, for convenience, as the inverse of the donor lifetime and $p(k_d)$ is the distribution of donor excited state decay rates. For the donor-acceptor labelled system the excited state decay is given as

$$I_{da}(t_{TCSPC}) = \int_0^{\infty} \int_0^{\infty} P(k_d, k_{ET}) \cdot e^{-(k_d+k_{ET}) \cdot t_{TCSPC}} dk_d dk_{ET} \quad (11.19)$$

where k_{ET} is the energy transfer rate given by the Förster equation. The two-dimensional distribution $p(k_d, k_{ET})$ describes the distribution of donor rates and energy-transfer rates. The distribution $p(k_d, k_{ET})$ is usually approximated in one-dimensional analyses as separate one-dimensional distributions giving rise to a “non-associative” model:

$$I_{da}(t_{TCSPC}) = \int_0^{\infty} P(k_d) e^{-k_d \cdot t_{TCSPC}} dk_d \cdot \int_0^{\infty} P(k_{ET}) e^{-k_{ET} \cdot t_{TCSPC}} dk_{ET} \quad (11.20)$$

This assumes that every subpopulation responsible for a different donor rate has the same energy-transfer rate distribution. The pair distance distribution is then calculated from the rate distribution according to the Förster equation [39]. Although this approximation results in significant computational advantages, the underlying assumption is not generally applicable. For example, a partially folded state and the unfolded state may be equally populated and the donor may exhibit different excited state lifetimes and a different donor-acceptor distance in each state. Scenarios such as this become especially likely at early times in folding reactions where marginally populated partially folded intermediates may interconvert rapidly. Discriminating these sub-populations is one of the goals of continuous-flow FRET studies. An analysis employing this 2D MEM approach was applied to the early steps in the folding of a TIM barrel protein (Fig. 11.13).

Although the FRET efficiencies were low and not ideal, the algorithm was able to discriminate two sub-populations. The main limitation of the 2D MEM approach is that the accuracy at low FRET efficiencies (e.g., 20 % and lower) is significantly reduced because of insufficient information in the data.

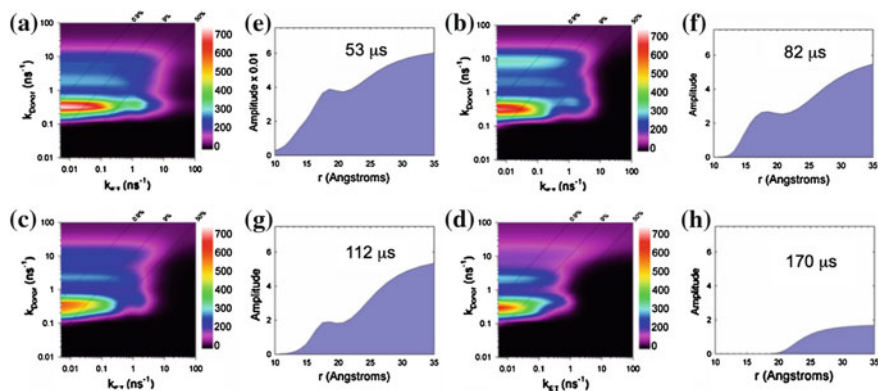


Fig. 11.13 2D MEM analysis at various time points during refolding of a TIM barrel protein. Used with permission [69]. Copyright—2008 by The National Academy of Sciences of the USA

One workaround to this limitation of the 2D MEM analysis [69] is to include an additional experimental axis or dimension such as the acceptor excited state decay. In preliminary tests this was found to yield significantly more reliable distribution functions in the low FRET efficiency tails of distributions. The computational cost of including the additional dimension scales non-linearly although the 3D MEM approach is within reach of current available computational power. The only potential drawback to MEM approaches is that these do not currently consider the diffusion of donor and acceptor chromophores during the excited state lifetime of the donor. However, for sufficiently large Förster distances and short lifetimes, this may still provide significant insights into the sub-populations present during a microsecond kinetic reaction.

11.5 Future Prospects

Significant advances in microfluidic technology have taken place over the past 5 years. Sample consumption, time resolution and temporal dynamic range have improved and the availability of simulation CFD software and microfabrication tools suggests that these advances will continue. These devices and TCSPC detection are used by a relatively small number of laboratories but the robustness of the devices and decreasing cost of TCSPC instrumentation point to increased adoption by the biochemistry community. These tools are likely to play an increasingly important role in FRET studies delineating enzyme mechanisms, protein-protein/RNA/DNA interactions and in enzymatic assays.

Acknowledgments The authors would like to thank McKenzie Davies for sharing representative data for the TCSPC analysis software figure, Brian Mackness and Jill Zitzewitz for helpful discussions and editing, and Bob Matthews for helpful discussions and support. This work was

supported by NSF grants DBI1353942 to O. Bilsel and J.B. Perot and MCB1121942 to C.R. Matthews and O. Bilsel and NIH grant GM23303 to C.R. Matthews and O. Bilsel.

References

1. K.N. Aprilakis, H. Taskent, D.P. Raleigh, Use of the novel fluorescent amino acid p-cyanophenylalanine offers a direct probe of hydrophobic core formation during the folding of the N-terminal domain of the ribosomal protein L9 and provides evidence for two-state folding. *Biochemistry* **46**, 12308–12313 (2007)
2. W. Becker, *Advanced Time-Correlated Single-Photon Counting Techniques* (Springer, Berlin, 2005)
3. W. Becker, *The bh TCSPC Handbook*, 5th edn. Becker & Hickl GmbH (2012), www.becker-hickl.com, printed copies available from Becker & Hickl GmbH
4. W. Becker, B. Su, K. Weisshart, O. Holub, FLIM and FCS detection in laser-scanning microscopes: increased efficiency by GaAsP hybrid detectors. *Microsc. Res. Tech.* **74**, 804–811 (2011)
5. J.M. Beechem, E. Haas, Simultaneous determination of intramolecular distance distributions and conformational dynamics by global analysis of energy transfer measurements. *Biophys. J.* **55**, 1225–1236 (1989)
6. J.M. Beechem, Global analysis of biochemical and biophysical data. *Methods Enzymol.* **210**, 37–54 (1992)
7. J.M. Beechem, Picosecond fluorescence decay curves collected on millisecond time scale: direct measurement of hydrodynamic radii, local/global mobility, and intramolecular distances during protein-folding reactions. *Methods Enzymol.* **278**, 24–49 (1997)
8. Y. Bellouard, T. Colomb, C. Depeursinge, M. Dugan, A.A. Said, P. Bado, Nanoindentation and birefringence measurements on fused silica specimen exposed to low-energy femtosecond pulses. *Opt. Express* **14**, 8360–8366 (2006)
9. O. Bilsel, L. Yang, J.A. Zitzewitz, J.M. Beechem, C.R. Matthews, Time-resolved fluorescence anisotropy study of the refolding reaction of the alpha-subunit of tryptophan synthase reveals nonmonotonic behavior of the rotational correlation time. *Biochemistry* **38**, 4177–4187 (1999)
10. O. Bilsel, C. Kayatekin, L.A. Wallace, C.R. Matthews, A microchannel solution mixer for studying microsecond protein folding reactions. *Rev. Sci. Instrum.* **76**, 014302 (2005)
11. D.J. Birch, D. McLoskey, A. Sanderson, K. Suhling, A.S. Holmes, Multiplexed time-correlated single-photon counting. *J Fluoresc* **4**, 91–102 (1994)
12. J.C. Brochon, Maximum entropy method of data analysis in time-resolved spectroscopy. *Methods Enzymol.* **240**, 262–311 (1994)
13. Y. Chen, A. Periasamy, Characterization of two-photon excitation fluorescence lifetime imaging microscopy for protein localization. *Microsc. Res. Tech.* **63**, 72–80 (2004)
14. R.B. Dyer, E.B. Brauns, Laser-induced temperature jump infrared measurements of RNA folding. *Methods Enzymol.* **469**, 353–372 (2009)
15. W.A. Eaton, V. Munoz, S.J. Hagen, G.S. Jas, L.J. Lapidus, E.R. Henry, J. Hofrichter, Fast kinetics and mechanisms in protein folding. *Annu. Rev. Biophys. Biomol. Struct.* **29**, 327–359 (2000)
16. T. Egawa, J.L. Durand, E.Y. Hayden, D.L. Rousseau, S.R. Yeh, Design and evaluation of a passive alcove-based microfluidic mixer. *Anal. Chem.* **81**, 1622–1627 (2009)
17. E.L. Elson, Fluorescence correlation spectroscopy: past, present, future. *Biophys. J.* **101**, 2855–2870 (2011)
18. S. Felekyan, H. Sanabria, S. Kalinin, R. Kühnemuth, C.A. Seidel, Analyzing Förster resonance energy transfer with fluctuation algorithms. *Methods Enzymol.* **519**, 39–85 (2013)

19. J.J. Fisz, Fluorescence polarization spectroscopy at combined high-aperture excitation and detection: application to one-photon-excitation fluorescence microscopy. *J. Chem. Phys. A* **111**, 8606–8621 (2007)
20. F. Gai, D. Du, Y. Xu, Infrared temperature-jump study of the folding dynamics of alpha-helices and beta-hairpins. *Methods Mol. Biol.* **350**, 1–20 (2007)
21. Y. Gambin, C. Simonnet, V. VanDelinder, A. Deniz, A. Groisman, Ultrafast microfluidic mixer with three-dimensional flow focusing for studies of biochemical kinetics. *Lab Chip* **10**, 598–609 (2010)
22. Y. Gambin, V. VanDelinder, A.C. Ferreon, E.A. Lemke, A. Groisman, A.A. Deniz, Visualizing a one-way protein encounter complex by ultrafast single-molecule mixing. Macmillan Publishers Ltd, *Nat. Methods* **8**, 239–241 (2011)
23. M. Gentin, M. Vincent, J.C. Brochon, A.K. Livesey, N. Cittanova, J. Gallay, Time-resolved fluorescence of the single tryptophan residue in rat alpha-fetoprotein and rat serum albumin: analysis by the maximum-entropy method. *Biochemistry* **29**, 10405–10412 (1990)
24. R. Gilmanishin, S. Williams, R.H. Callender, W.H. Woodruff, R.B. Dyer, Fast events in protein folding: relaxation dynamics of secondary and tertiary structure in native apomyoglobin. *Proc. Natl. Acad. Sci. U.S.A.* **94**, 3709–3713 (1997)
25. E. Haas, Ensemble FRET methods in studies of intrinsically disordered proteins. *Methods Mol. Biol.* **895**, 467–498 (2012)
26. S.J. Hagen, J. Hofrichter, A. Szabo, W.A. Eaton, Diffusion-limited contact formation in unfolded cytochrome c: estimating the maximum rate of protein folding. *Proc. Natl. Acad. Sci. U.S.A.* **93**, 11615–11617 (1996)
27. K.M. Hamadani, S. Weiss, Nonequilibrium single molecule protein folding in a coaxial mixer. *Biophys. J.* **95**, 352–365 (2008)
28. D.F. Hansen, H. Feng, Z. Zhou, Y. Bai, L.E. Kay, Selective characterization of microsecond motions in proteins by NMR relaxation. *J. Am. Chem. Soc.* **131**, 16257–16265 (2009)
29. E.B. Ishay, G. Hazan, G. Rahamim, D. Amir, E. Haas, An instrument for fast acquisition of fluorescence decay curves at picosecond resolution designed for “double kinetics” experiments: application to fluorescence resonance excitation energy transfer study of protein folding. *Rev. Sci. Instrum.* **83**, 084301 (2012)
30. K.C. Jones, C.S. Peng, A. Tokmakoff, Folding of a heterogeneous beta-hairpin peptide from temperature-jump 2D IR spectroscopy. *Proc. Natl. Acad. Sci. U.S.A.* **110**, 2828–2833 (2013)
31. S.V. Kathuria, L. Guo, R. Graceffa, R. Barrea, R.P. Nobrega, C.R. Matthews, T.C. Irving, O. Bilsel, Minireview: structural insights into early folding events using continuous-flow time-resolved small-angle X-ray scattering. *Biopolymers* **95**, 550–558 (2011)
32. S.V. Kathuria, C. Kayatekin, R. Barrea, E. Kondrashkina, R. Graceffa, L. Guo, R.P. Nobrega, S. Chakravarthy, C.R. Matthews, T.C. Irving, O. Bilsel, Microsecond barrier-limited chain collapse observed by time-resolved FRET and SAXS. *J. Mol. Biol.* **426**(9), 1980–1994 (2014)
33. S.V. Kathuria, A. Chan, R. Graceffa, R. Paul Nobrega, C. Robert Matthews, T.C. Irving, B. Perot, O. Bilsel, Advances in turbulent mixing techniques to study microsecond protein folding reactions. *Biopolymers* **99**, 888–96 (2013)
34. B.A. Kelch, D.L. Makino, M. O’Donnell, J. Kuriyan, How a DNA polymerase clamp loader opens a sliding clamp. *Science* **334**, 1675–1680 (2011)
35. T. Kimura, J.C. Lee, H.B. Gray, J.R. Winkler, Site-specific collapse dynamics guide the formation of the cytochrome c’ four-helix bundle. *Proc. Natl. Acad. Sci. U.S.A.* **104**, 117–122 (2007)
36. M. Köllner, J. Wolfrum, How many photons are necessary for fluorescence-lifetime measurements? *Phys. Chem. Lett.* **200**, 199–204 (1992)
37. J. Kubelka, W.A. Eaton, J. Hofrichter, Experimental tests of villin subdomain folding simulations. *J. Mol. Biol.* **329**, 625–630 (2003)
38. A.T.N. Kumar, L. Zhu, J.F. Christian, A.A. Demidov, P.M. Champion, On the rate distribution analysis of kinetic data using the maximum entropy method: applications to myoglobin relaxation on the nanosecond and femtosecond timescales. *J. Phys. Chem. B* **105**, 7847–7856 (2001)

39. J.R. Lakowicz, *Principles of Fluorescence Spectroscopy*, 3rd edn. (Springer, Berlin, 2006)
40. T.J. Lane, D. Shukla, K.A. Beauchamp, V.S. Pande, To milliseconds and beyond: challenges in the simulation of protein folding. *Curr. Opin. Struct. Biol.* **23**, 58–65 (2013)
41. L.J. Lapidus, S. Yao, K.S. McGarrity, D.E. Hertzog, E. Tubman, O. Bakajin, Protein hydrophobic collapse and early folding steps observed in a microfluidic mixer. *Biophys. J.* **93**, 218–224 (2007)
42. Y. Li, D. Zhang, X. Feng, Y. Xu, B.F. Liu, A microsecond microfluidic mixer for characterizing fast biochemical reactions. *Talanta* **88**, 175–180 (2012)
43. K. Lindorff-Larsen, S. Piana, R.O. Dror, D.E. Shaw, How fast-folding proteins fold. *Science* **334**, 517–520 (2011)
44. F. Liu, M. Nakaema, M. Gruebele, The transition state transit time of WW domain folding is controlled by energy landscape roughness. *J. Chem. Phys.* **131** (2009)
45. A.K. Livesey, J.C. Brochon, Analyzing the distribution of decay constants in pulse-fluorimetry using the maximum entropy method. *Biophys. J.* **52**, 693–706 (1987)
46. K. Malecha, L.J. Golonka, J. Bałdyga, M. Jasińska, P. Sobieszuk, Serpentine microfluidic mixer made in LTCC. *Sens. Actuators, B* **143**, 400–413 (2009)
47. V. Munoz, P.A. Thompson, J. Hofrichter, W.A. Eaton, Folding dynamics and mechanism of beta-hairpin formation. *Nature* **390**, 196–199 (1997)
48. M.R. Otto, M.P. Lillo, J.M. Beechem, Resolution of multiphasic reactions by the combination of fluorescence total-intensity and anisotropy stopped-flow kinetic experiments. *Biophys. J.* **67**, 2511–2521 (1994)
49. S.A. Pabit, S.J. Hagen, Laminar-flow fluid mixer for fast fluorescence kinetics studies. *Biophys. J.* **83**, 2872–2878 (2002)
50. S.A. Pabit, J.L. Sutton, H. Chen, L. Pollack, Role of ion valence in the submillisecond collapse and folding of a small RNA domain. *Biochemistry* **52**, 1539–1546 (2013)
51. A.G. Palmer, Nmr probes of molecular dynamics: overview and comparison with other techniques. *Annu. Rev. Biophys. Biomol. Struct.* **30**, 129–155 (2001)
52. H.Y. Park, X. Qiu, E. Rhoades, J. Korlach, L.W. Kwok, W.R. Zipfel, W.W. Webb, L. Pollack, Achieving uniform mixing in a microfluidic device: hydrodynamic focusing prior to mixing. *Anal. Chem.* **78**, 4465–4473 (2006)
53. C.M. Phillips, Y. Mizutani, R.M. Hochstrasser, Ultrafast thermally induced unfolding of RNase A. *Proc. Natl. Acad. Sci. U.S.A.* **92**, 7292–7296 (1995)
54. L. Pollack, M.W. Tate, N.C. Darnton, J.B. Knight, S.M. Gruner, W.A. Eaton, R.H. Austin, Compactness of the denatured state of a fast-folding protein measured by submillisecond small-angle x-ray scattering. *Proc. Natl. Acad. Sci. U.S.A.* **96**, 10115–10117 (1999)
55. V. Ratner, D. Amir, E. Kahana, E. Haas, Fast collapse but slow formation of secondary structure elements in the refolding transition of *E. coli* adenylate kinase. *J. Mol. Biol.* **352**, 683–699 (2005)
56. P. Regenfuss, R.M. Clegg, M.J. Fulwyler, F.J. Barrantes, T.M. Jovin, Mixing liquids in microseconds. *Rev. Sci. Instrum.* **56**, 283 (1985)
57. H. Roder, K. Maki, H. Cheng, Early events in protein folding explored by rapid mixing methods. *Chem. Rev.* **106**, 1836–1861 (2006)
58. J.M. Rogers, L.G. Lippert, F. Gai, Non-natural amino acid fluorophores for one- and two-step fluorescence resonance energy transfer applications. *Anal. Biochem.* **399**, 182–189 (2010)
59. F. Schonfeld, V. Hessel, C. Hofmann, An optimised split-and-recombine micro-mixer with uniform ‘chaotic’ mixing. *Lab Chip* **4**, 65–69 (2004)
60. M.C. Shastry, S.D. Luck, H. Roder, A continuous-flow capillary mixing method to monitor reactions on the microsecond time scale. *Biophys. J.* **74**, 2714–2721 (1998)
61. J. Skilling, R.K. Bryan, Maximum entropy image reconstruction: general algorithm. *Mon. Not. R. Astron. Soc.* **211**, 111–124 (1984)
62. T.R. Sosnick, D. Barrick, The folding of single domain proteins—have we reached a consensus? *Curr. Opin. Struct. Biol.* **21**, 12–24 (2011)
63. A.D. Stroock, S.K.W. Dertinger, A. Ajdari, I. Mezic, H.A. Stone, G.M. Whitesides, Chaotic mixer for microchannels. *Science* **295**, 647–651 (2002)

64. S. Takahashi, S.R. Yeh, T.K. Das, C.K. Chan, D.S. Gottfried, D.L. Rousseau, Folding of cytochrome c initiated by submillisecond mixing. *Nat. Struct. Biol.* **4**, 44–50 (1997)
65. H. Taskent-Sezgin, P. Marek, R. Thomas, D. Goldberg, J. Chung, I. Carrico, D.P. Raleigh, Modulation of p-cyanophenylalanine fluorescence by amino acid side chains and rational design of fluorescence probes of alpha-helix formation. *Biochemistry* **49**, 6290–6295 (2010)
66. D. Thirumalai, B.-Y. Ha, Statistical mechanics of semiflexible chains: a meanfield variational approach. arXiv:cond-mat/9705200 (1997)
67. P.A. Thompson, W.A. Eaton, J. Hofrichter, Laser temperature jump study of the helix \rightleftharpoons coil kinetics of an alanine peptide interpreted with a ‘kinetic zipper’ model. *Biochemistry* **36**, 9200–9210 (1997)
68. C.T. Wang, Y.C. Hu, T.Y. Hu, Biophysical micromixer. *Sens. (Basel)* **9**, 5379–5389 (2009)
69. Y. Wu, E. Kondrashkina, C. Kayatekin, C.R. Matthews, O. Bilse, Microsecond acquisition of heterogeneous structure in the folding of a TIM barrel protein. *Proc. Natl. Acad. Sci. U.S.A.* **105**, 13367–13372 (2008)
70. B. Wunderlich, D. Nettels, S. Benke, J. Clark, S. Weidner, H. Hofmann, S.H. Pfeil, B. Schuler, Microfluidic mixer designed for performing single-molecule kinetics with confocal detection on timescales from milliseconds to minutes. Macmillan Publishers Ltd, *Nat. Protoc.* **8**, 1459–1474 (2013)
71. W.Y. Yang, M. Gruebele, Folding at the speed limit. *Nature* **423**, 193–197 (2003)
72. G. Zoldak, J. Stigler, B. Pelz, H. Li, M. Rief, Ultrafast folding kinetics and cooperativity of villin headpiece in single-molecule force spectroscopy. *Proc. Natl. Acad. Sci. U.S.A.* **110**, 18156–18161 (2013)